Editors' Suggestion

Active gel theory for cell migration with two myosin isoforms

Nils O. Winkler [1], Oliver M. Drozdowski [1,2], Falko Ziebert [1], and Ulrich S. Schwarz [1,2,*]

[1]*Institute for Theoretical Physics and Bioquant, Heidelberg University, 69120 Heidelberg, Germany*
[2]*Max Planck School Matter to Life, Heidelberg University, 69120 Heidelberg, Germany*

Myosin II molecular motors slide actin filaments relatively to each other and are essential for force generation, motility, and mechanosensing in animal cells. For nonmuscle cells, evolution has resulted in three different isoforms, which have different properties concerning the motor cycle and also occur in different abundances in the cells, but their respective biological and physical roles are not fully understood. Here we use active gel theory to demonstrate the complementary roles of isoforms A and B for cell migration. We first show that our model can be derived both from coarse-graining kinetic equations and from nonequilibrium thermodynamics as the macroscopic limit of a two-component Tonks gas. We then parametrize the model and show that motile solutions exist, in which the more abundant and more dynamic isoform A is localized to the front and the stronger isoform B to the rear, in agreement with experiments. Exploring parameter space beyond the isoform parameters typical for animal cells, we also find cell oscillations in length and velocity, which might be realized for genetically engineered systems. We also describe an analytical solution for the stiff limit, which then is used to calculate a state diagram, and the effect of actin polymerization at the boundaries that leads to an imperfect pitchfork bifurcation. Our findings highlight the importance of including isoform-specific molecular details to describe whole cell behavior.

I. INTRODUCTION

Cell migration is an essential process for any living organism. In multicellular animals like humans, it is important mainly for embryonic development [1], wound healing [2], and the immune response [3] but also for the spread of cancer [4]. It is strongly linked to the underlying molecular processes, because cells have to generate force and movement that is converted into consistent migration on the cell scale. This function is provided by the cytoskeleton, a collection of polymer networks. Cells can push their envelope forward by polymerization of these filaments. They also can generate pulling forces by sliding them relative to each other with molecular motors. For animal cells, pushing and pulling forces are generated mainly by actin filaments and myosin II molecular motors. In cell migration, they go hand in hand, because the actin networks generated by polymerization are pulled backward by myosin II motors. The resulting retrograde flow is then transmitted to the substrate by adhesions and thus generates forward motion of the cell [5]. Migration requires a cyclic process that converts energy provided in the form of ATP into force and movement. Moreover, initiation of motility requires a symmetry break between front and back, which can be either spontaneous or driven by some external cue [6–8]. Usually this break of symmetry is related to activation of the Rac/Cdc42 and RhoA pathways, which for quantitative experiments can be controlled by optogenetics [9–11].

In nonmuscle animal cells contractile stress for cell motility is produced by motor proteins of the nonmuscle myosin II (NMII) family [12]. Evolution has resulted in three isoforms, namely NMIIA, NMIIB, and NMIIC [13]. After activation of the Rho pathway, the myosin motors are assembled into minifilaments that typically mix different isoforms [13,14]. These minifilaments then bind to the actin cytoskeleton, generate stress, and at the same time are advected with the resulting cytoskeletal flow. In the case of asymmetric contractile stress distributions, the cell is polarized and starts migrating. While NMIIA is most abundant and propels loads the quickest along actin filaments, NMIIB is the strongest due to its higher duty ratio; NMIIC seems to have little relevance for cell migration, also due to its low abundance [15,16]. Recent experiments have shown that in a migrating cell the isoforms A and B are not distributed equally [14,15]. While the more abundant and more dynamic isoform A localizes more at the leading edge, the stronger isoform B accumulates towards the trailing edge (cf. Fig. 1).

In the following, we will define and analyze a model that considers the complementary roles played by the two dominant isoforms A and B. We use active gel theory, which models the contractile actomyosin network as an active viscous material and thus is a natural approach to describe flowing actin networks as the physical basis of cell crawling [17,18]. In principle, active gel theory can describe the effects of both actin polymerization and myosin-based contractility, but seminal work has shown that contractility alone is sufficient to explain cell migration [19–21]. While this minimal model leads to a supercritical pitchfork bifurcation towards a motile state, more recently it was shown that a subcritical

---

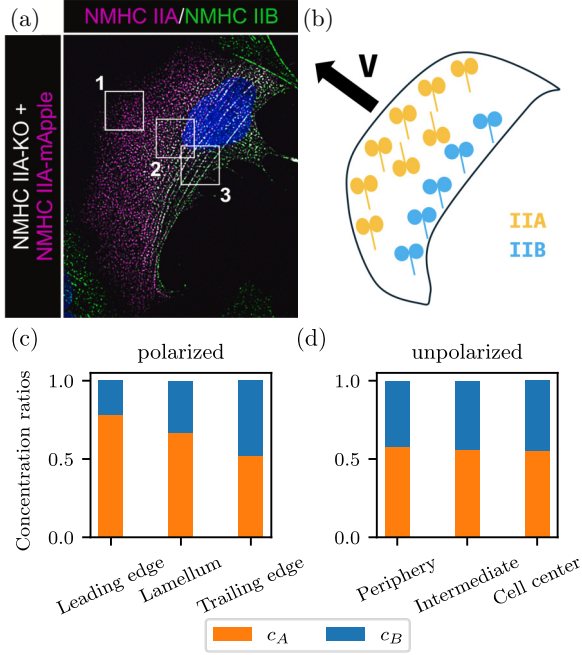*Contact author: schwarz@thphys.uni-heidelberg.de

024413-1

FIG. 1. NMII isoform distributions in cells. (a) Microscopy image of a U2OS cell with exogenous NMIIA (magenta) and endogenous NMIIB (green). Modified from Ref. [15]. (b) Schematic sketch of a cell indicating NMII isoform distribution and net cell movement. [(c) and(d)] Experimental concentration ratios of NMIIA and NMIIB within different cell compartments [(c) along the axis of polarization and (d) unpolarized cell]. Adapted from Ref. [15]. While both isoforms are equally distributed in an unpolarized cell, in a moving cell NMIIA and NMIIB enrich at the leading and trailing edges, respectively.

pitchfork bifurcation and bistability can be obtained when including a nonlinearity in the diffusion behavior, which can be derived from the physics of a van der Waals fluid [22].

Here we extend this approach to a theory for two species of NMII. Motivated by experiments by Weissenbruch *et al.* [15,16], we incorporate phenomenological binding kinetics, including the competition of isoforms A and B for binding sites on actin filaments. This amounts to a volume exclusion interaction and results in an effective nonlinear diffusion of myosins as known from the Tonks gas [23]. Our new model explains the experimentally observed distributions of NMIIA and NMIIB in a polarized migrating cell. Exploring the parameter space we can describe four different modes of cell motility: nonmotile cells, decaying and stable pull-push velocity oscillations, and motile steady migration. Using both numerical simulations and analytical theory, we can obtain a complete phase diagram for our model.

The paper is organized as follows. We will start by defining the mathematical model based on active gel theory introducing the constitutive relation for stress. From binding kinetics we derive an effective nonlinear diffusion and demonstrate its consistency with the thermodynamics of a Tonks gas of two species. We then investigate the resulting closed boundary value problem and recapture experimental results in steady state. Lifting the constraint of steady state we demonstrate an

oscillation mechanism for cell length and velocity. Next we introduce a limiting case which can be treated analytically and for which we present a phase diagram indicating four different modes of motility. Last, we demonstrate the effect of actin polymerization.

II. MINIMAL CELL MODEL WITH TWO MYOSIN ISOFORMS

A. Geometry and mechanics of the cell

Our one-dimensional model considers an infinitely compressible active gel. As commonly assumed [20,22,24], the active contractile stress depends linearly on the motor concentration c, $\sigma_{act} = -\chi c$, resulting in the constitutive relation

$$\eta \partial_x v(x, t) = \sigma(x, t) - \chi_A c_A(x, t) - \chi_B c_B(x, t). \quad (1)$$

Here $v(x, t)$ is the velocity of the actin flow and η the viscosity. The right-hand side contains the total stress $\sigma(x, t)$ and the active stresses caused by the myosin concentrations $c_A(x, t), c_B(x, t)$ of the two isoforms. The minus signs relate to contraction and the prefactors χ_A, χ_B quantify the contractility of the species. Since the cell is adhering to the substrate, we assume homogeneous viscous drag and get the force balance

$$\partial_x \sigma = \xi v, \quad (2)$$

where ξ is a friction coefficient. The cell occupies the range $x \in [l_-, l_+]$ and hence its length is given by $L(t) = l_+(t) - l_-(t)$ and its midpoint velocity by $\dot{G}(t) = \frac{d}{dt}(l_+(t) + l_-(t))/2$. We use an elastic boundary condition, $\sigma(l_\pm, t) = -k(L(t) - L_0)/L_0$, that models membrane tension and all other restoring forces limiting the cell size [20–22]. Here k is the effective spring constant of the cell and L_0 its homeostatic length.

B. Myosin motor binding kinetics

Myosin motors generate contractile forces by binding to actin. Informed by the myosin cross-bridge cycle [25–28], we can formulate equations for their dynamic behavior. Although the cross-bridge cycle consists of multiple steps, we will solely distinguish between motors that are either attached to (index a) or detached from (index d) actin filaments to create an effective two-state model as considered in Refs. [20,22,29].

In the unbound state, the motors can freely move inside the cytoplasm with diffusion constant $\tilde{D}$ and bind to actin at a rate k_{on}. The binding process is subject to volume exclusion effects, i.e., there must be a free spot available on the actin filament to be able to bind. This is modeled by introducing a saturation concentration c_∞. When it is reached locally, no more binding is possible. The attached proteins move with the (retrograde) actin flow by advection with the velocity v. Since the cytoplasm is considered as a reservoir for the motors, the detachment rate k_{off} is assumed to be independent of any interaction effects. In general, the binding rates are specific for each isoform ($k_{A,on/off} \neq k_{B,on/off}$). In contrast, both the diffusion coefficient and the saturation concentration are mostly determined by the size of the protein which is the same

for both isoforms. This leads to the following two differential equations per isoform

$$\partial_t c_{i,a} + \partial_x(v c_{i,a}) = R(c_{i,a}, c_{i,d}), \tag{3a}$$

$$\partial_t c_{i,d} - \tilde{D}\partial_x^2 c_{i,d} = -R(c_{i,a}, c_{i,d}), \tag{3b}$$

$$R(c_{i,a}, c_{i,d}) = \frac{k_{i,\text{on}}}{c_\infty}(c_\infty - (c_{i,a} + c_{j,a}))c_{i,d} - k_{i,\text{off}}\, c_{i,a}. \tag{3c}$$

Here $R(c_{i,a}, c_{i,d})$ is a nonlinear function describing the reaction kinetics and i, j refer to isoforms A and B, respectively. For the cellular behavior on the timescale of interest here, we do not include a production of myosin inside the cell but rather require the total myosin concentration of each isoform to remain constant. This requirement then leads to no-flux boundary conditions for the two species, $\partial_x c_{A,B}(l_\pm, t) = 0$.

We now simplify the problem, as previously proposed for similar models [20,22]. First, we assume local chemical equilibrium, $R(c_a, c_d) = 0$, and obtain expressions for the detached motors

$$c_{i,d} = \frac{1}{K_i} \cdot \frac{c_{i,a} c_\infty}{c_\infty - (c_{i,a} + c_{j,a})}, \tag{4}$$

where $K_i = k_{i,\text{on}}/k_{i,\text{off}}$ is the dissociation constant. Second, we take the limit of fast binding and fast diffusion ($K_A, \tilde{D} \to \infty$) with $\tilde{D}/K_A \to D_A$ and $\tilde{D}/K_B \to D_A K_r$, where we introduced $K_r = K_A/K_B$ as the ratio of the dissociation constants of the two isoforms. Adding now Eqs. (3a) and (3b) and inserting Eq. (4), we obtain one advection-diffusion equation for each isoform, describing the effective dynamics of the bound myosin motors,

$$\partial_t c_A = -\partial_x(v c_A) + D_A \partial_x \mathcal{D}_A(c_A, c_B), \tag{5a}$$

$$\partial_t c_B = -\partial_x(v c_B) + D_A K_r \partial_x \mathcal{D}_B(c_A, c_B). \tag{5b}$$

Above, we have already dropped the indices a and in the following motors always refer to attached motors. The fact that the detached motor concentration drops out comes at the cost of concentration-dependent diffusion coefficients, which read

$$\begin{aligned}\mathcal{D}_i &= D_{ii}\partial_x c_i + D_{ij}\partial_x c_j \\ &= \frac{c_\infty(c_\infty - c_j)}{(c_\infty - (c_A + c_B))^2}\partial_x c_i + \frac{c_\infty c_i}{(c_\infty - (c_A + c_B))^2}\partial_x c_j. \end{aligned} \tag{6}$$

The diffusion for both (actin-bound) myosin isoforms is nonlinear in the concentration, and it shows cross-diffusion properties, i.e., a gradient of isoform B influences the dynamics of isoform A and vice versa. Note that for $c_A = c_B = c/2$, we obtain the model for a single motor species interacting through volume exclusion [22]. The concentration dependence in the prefactors of the gradients in Eq. (6) arise from the excluded volume interaction, quantified by the saturation concentration c_∞. For concentrations approaching saturation the diffusion diverges, whereas for $c_A, c_B \ll c_\infty$ we recover concentration-independent diffusion constants and vanishing cross-coupling.

Both nonlinear diffusion and cross-diffusion have been introduced and analyzed for other systems, the former for instance for bacterial growth [30] and crowded motor protein systems [22,31], the latter in micelle solutions [32], protein-polymer mixtures [33], and reaction-diffusion systems [34]. We here intend to investigate their effects in the context of intracellular flow, internal cell organization, cell polarization, and cell motility.

C. Myosin as Tonks gas

The nonlinear, concentration-dependent diffusion of Eq. (6) can also be derived using arguments from classical irreversible thermodynamics. Assuming a homogeneous "gas" of two species, A and B, of hard spheres interacting only sterically (Tonks gas [23]), one finds a free energy density of

$$\begin{aligned}f(c_A, c_B) = RT\Bigg[&c_A \ln\left(\frac{c_A}{c_\infty - c_A - c_B}\right) \\ &+ c_B \ln\left(\frac{c_B}{c_\infty - c_A - c_B}\right) \\ &+ c_\infty \ln\left(1 - \frac{c_A + c_B}{c_\infty}\right)\Bigg]. \end{aligned} \tag{7}$$

Here R is the universal gas constant and T temperature. This expression can be derived by either using a density functional theory ansatz [35–38] or statistical arguments similar to Flory-Huggins theory [39,40].

The first two terms in Eq. (7) arise from a Tonks gas with two different species of spheres. However, the last term takes its form due to the introduction of holes into the system. These holes effectively constitute a third species. Besides, the cytosol and actin network are considered as an additional dense solvent background, whose influence can be neglected due to the myosin size. The saturation concentration then reads $c_\infty = c_A + c_B + c_{\text{holes}}$. In the dilute limit, i.e., for large c_∞, the last term reduces to the sum of c_A and c_B which resembles the free energy of the combination of two individual Tonks gases. Hence, the last term can be interpreted as the correlation between both species at concentrations of an order of magnitude similar to the saturation.

Within nonequilibrium thermodynamics, fluxes are driven by gradients in conjugate thermodynamic forces. The relevant couple in our case is particle flux and chemical potential. We use standard linear theory to express particle fluxes as a linear expansion of all thermodynamic forces, introducing the phenomenological Onsager coefficients L_{ij} that in turn can also depend on the thermodynamic variables. Doing so we can relate the particle flux to the diffusion within the multicomponent mixture

$$\frac{1}{RT}\sum_{j\in\{A,B\}} L_{ij}\left(-\frac{\partial \mu_j}{\partial x}\right) = -\sum_{j\in\{A,B\}} D_{ij}\left(\frac{\partial c_j}{\partial x}\right), \tag{8}$$

where μ is the chemical potential, L_{ij} is the matrix of phenomenological coefficients, and D_{ij} the diffusion matrix. Obtaining the chemical potential from the free energy via $\mu_j = \partial f/\partial c_j$, we get the same diffusion coefficients as derived from binding kinetics, Eq. (6), if the matrix of phenomenological coefficients is

$$\mathbf{L} = \frac{c_\infty}{c_\infty - c_A - c_B}\begin{pmatrix} c_A & 0 \\ 0 & c_B \end{pmatrix}. \tag{9}$$

The concentration-dependent prefactor of Eq. (9) arises due to the excluded volume interaction. It is necessary in order for the steric repulsion not to vanish in the limiting case of one of the species' concentration vanishing. Note that a species is not only affected by the excluded volume with itself but also with the other species. For the dilute limit, which implies a large saturation concentration, the prefactor converges to unity and one recovers the diagonal matrix $L_{ij} = c_i\delta_{ij}$ as typically used for the diffusion of different species without explicit volume exclusion interactions, cf. e.g., Ref. [41].

D. Full boundary value problem

By combining the myosin dynamics Eq. (5), with diffusion coefficients given by Eq. (6), with the constitutive relation, Eq. (1), and the force balance, Eq. (2), we can formulate the full boundary value problem.

We introduce dimensionless variables and rescale length and position by the cell length L_0, time by L_0^2/D_A and contractile stress by the spring constant k. The concentrations are normalized using the initial average concentration of isoform A, i.e., $c_A^0 = \int c_A dx/L_0$. The initial average concentration of B can then be calculated using the relative abundance $c_r = c_A^0/c_B^0$. Furthermore, we introduce $\mathcal{L} = \sqrt{\eta/(\xi L_0^2)}$ as the ratio of the viscous and the frictional length scales [42], the dimensionless contractility $P_i = \chi_i c_A^0/k$ of the two isoforms and the Péclet number $\mathrm{Pe} = k/(\xi D_A)$.

We then map the problem into internal coordinates $u = (x - l_-)/L \in [0, 1]$ to work on a fixed domain. The dimensionless boundary value problem then reads

$$-\frac{\mathcal{L}^2}{L^2}\partial_u^2\tilde{\sigma} + \tilde{\sigma} = P_A\tilde{c}_A + P_B\tilde{c}_B, \tag{10a}$$

$$\partial_t\tilde{c}_A = -\frac{1}{L}\partial_u(\tilde{v}\tilde{c}_A) + \frac{1}{L^2}\partial_u\mathcal{D}_A(\tilde{c}_A/L, \tilde{c}_B/L), \tag{10b}$$

$$\partial_t\tilde{c}_B = -\frac{1}{L}\partial_u(\tilde{v}\tilde{c}_B) + \frac{K_r}{L^2}\partial_u\mathcal{D}_B(\tilde{c}_A/L, \tilde{c}_B/L). \tag{10c}$$

Here $\tilde{c}_i(u,t) = L(t)c_i(u,t)$ and $\tilde{\sigma}(u,t) = L(t)\sigma(u,t)$ are rescaled concentrations and stress. Both myosin isoform are advected by the actin retrograde flow with $\tilde{v} = \frac{\mathrm{Pe}}{L^2}\partial_u\tilde{\sigma} - \dot{L}(u - \frac{1}{2}) - \dot{G}$. The elastic boundary condition reduces to $\tilde{\sigma}(u_\pm, t) = -L(t)(L(t) - 1)$ with $u_\pm \in \{0, 1\}$. The no-flux condition for the myosins is given by $\partial_u c_{A,B}(u_\pm, t) = 0$. The system of equations presented in Eq. (10) will now be analyzed in the following by continuation methods and direct numerical simulation. The corresponding computer code has been made publicly available [43]. The main parameters are Pe, P_A, P_B, K_r, c_∞, c_r. The meaning of $\mathcal{L}$ has been discussed before in Refs. [21,22].

III. RESULTS

A. Comparison to one-species models

As a background for the new two-species model, we briefly recall the basic features of the one-species model. As studied in Refs. [19,20], the model for one species and a constant diffusion coefficient allows for a supercritical pitchfork bifurcation from sessile to moving cells as a function of Pe. The instability is due to the motors being advected to the back by retrograde flow from where they pull further motors backward in a positive feedback loop. Because the motor distribution at the back can become unrealistically high in this model, excluded volume effects have been introduced, which imply nonlinear diffusion and smoothen the motor distribution [22]. It was also shown that attractive interactions, modeling myosin minifilament assembly, can render the bifurcation subcritical, thus leading to bistability and the possibility of optogenetic switching. More recently, it has been shown in a mathematically rigorous analysis that this subcritical bifurcation persists in a two-dimensional (2D) version of this model [44].

Here we are motivated by the experiments by Weissenbruch *et al.* [15,16], who have investigated the distributions of the isoforms NMIIA and NMIIB in polarized U2OS cells moving on a substrate in a steady fashion. As shown in Fig. 1, the more abundant, faster isoform A accumulates at the leading edge while the stronger, higher duty ratio NMIIB at the trailing edge. Therefore we now have generalized this model to two species. For the moment being, we did not include any attraction yet, thus our reference case is the Tonks gas and not the van der Waals fluid.

B. Model parameters

Informed by experimental data on crawling cells, we first estimate the parameters of our model. Due to $\xi \sim 2 \times 10^{14}$ Pa s m^{-1} [22,45], $\eta \sim 10^5$ Pa s [20,45], $k \sim 10^4$ Pa [16,46,47], and $L_0 \sim 20$ μm [20] we obtain a (squared) relative viscous length scale of $\mathcal{L}^2 = 1.25$. Using $D_A \sim 0.1 \times 10^{-12}$ m^2 s^{-1} [48–51], we infer the order of magnitude of the Péclet number to be Pe ~ 100.

The isoform-specific (off-)binding rates determine K_r, which in turn serves as a measure of relative diffusion. While the binding rates of both isoforms are equal ($k_{A,\mathrm{on}} = k_{B,\mathrm{on}} = 0.2$ s^{-1}), off-binding rates are $k_{A,\mathrm{off}} = 1.71$ s^{-1} and $k_{B,\mathrm{off}} = 0.35$ s^{-1} [28,29,52,53] leading to a relative diffusion of $K_r \approx 0.2$. The contractility parameters, as defined earlier, are of the order $P_i \sim 0.1$ [20]. Due to the different duty ratios of the isoforms A and B we find $P_B \approx 3.6 \cdot P_A$ [28] and, thus, choose $P_A = 0.05$ and $P_B = 0.18$. Last, following arguments from Ref. [22] we use $c_\infty = 4$ for the saturation concentration. The concentration ratio of $c_r \approx 1.5$ is taken from experiments [15].

C. Myosin isoform distributions in steadily moving cells

We solve the boundary value problem for steady states using the numerical continuation software *Auto07-p* [43,54]. The results for the parameters estimated above are shown in Fig. 2. Figures 2(a) and 2(b) show the bifurcation diagrams. Below a critical value of Pe$_{\mathrm{crit}} \approx 82$, the cell is in a sessile state with zero velocity [Fig. 2(a)] and at its homeostatic length [Fig. 2(b)]. The corresponding concentration profiles are shown in Fig. 2(c): They are flat and hence symmetric for both isoforms. In Fig. 2(c) we also show the total active stress $\sigma_{\mathrm{act}}(u) = -\chi_A c_A(u) - \chi_B c_B(u)$ as the dashed line, which
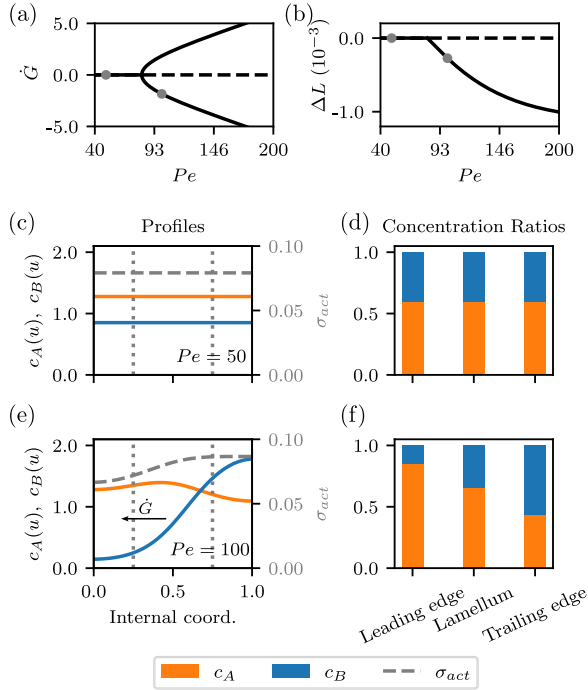
FIG. 2. Simulation results for steadily moving cells. (a) Super-critical pitchfork bifurcation of cell velocity $\dot{G}$ as a function of the Péclet number Pe (primary continuation parameter). Solid lines mark stable, dashed lines unstable solutions. (b) Deviation of the cell length from its homeostatic value $\Delta L = L - L_0$ as a function of Péclet number. (c) Myosin concentration profiles of the two iso-forms and the resulting total active stress σ_{act} of a sessile steady state. (d) The corresponding concentration ratios subdivided into three compartments as indicated by the gray dotted lines in (c). (e) Concentration profiles and total active stress for a motile steady state (cell velocity direction to the left indicated with arrow) and the corresponding concentrations ratios in (f). Parameters used: $\mathcal{L}^2 = 1.25$, $K_r = 0.2$, $P_A = 0.05$, $P_B = 0.18$, $c_\infty = 4$, $c_r = 1.5$.

obviously is also flat. We also define the concentration ratios as $c_i/(c_A + c_B)$, with $i = A, B$.

At the critical Péclet number, a supercritical pitchfork bifurcation occurs where the sessile state becomes unstable and stable motile steady states emerge. The two motile branches in Fig. 2(a) are $\pm$ symmetric and belong to the same, slightly contracted branch of the cell's length in Fig. 2(b). Whether one moves to the right or to the left is determined by the initial conditions. Due to the high dimensionality of our non-linear PDE system, analytical proof of attractor uniqueness is infeasible. However, Recho *et al.* [20] showed that in a similar single-species model, only the first supercritical pitch-fork bifurcation leads to stable modes. Given this similarity, we expect the same here. Numerical simulations from varied initial conditions revealed no evidence of additional stable branches.

In the steadily moving cell state beyond the bifurcation, the myosin distributions are asymmetric, as depicted in Fig. 2(e). This symmetry break in the concentrations induces a polarized active stress profile that initiates cell polarization and motility. In the shown example, the active stress is highest at the right edge ($u = 1$), inducing a retrograde flow of actin
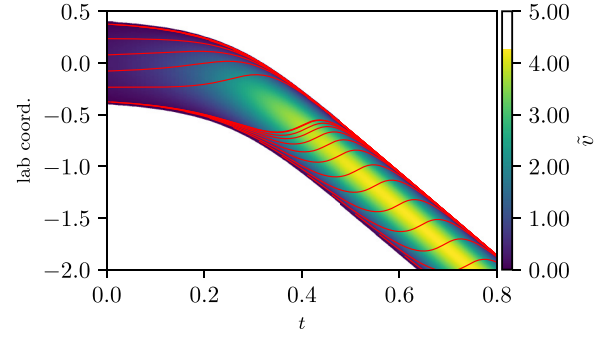

FIG. 3. Kymograph, i.e., trajectories in space and time, showing the advection through retrograde actin flow of a cell that approaches steady-state motility. The flow lines (red) are directed towards the rear end and the flow velocity reaches a maximum value of $\tilde{v}_{max} \sim 4.0 \times 10^{-2}$ μm s^{-1}.

to this end. Therefore, the cell moves to the left, like in the experimental examples from Fig. 1. The trailing edge is the locus of highest myosin concentration and, thus, highest active stress, in agreement to earlier theoretical works [20,21] as well as experimental findings [13,15,16].

As already discussed, the two myosin isoforms and hence the concentration ratio are homogeneously distributed within the sessile state, see Fig. 2(d). Comparing to Fig. 1(d), due to the lack of a polarization axis in the sessile state, we should identify the lamellum with the cell center and the region called "intermediate" region in Fig. 1(d), and both edges with the periphery. In the motile steady state the stronger isoform B sits in the back, while the more diffusive isoform A is displaced towards the front causing the varying concentration ratios as shown in Fig. 2(f). This redistribution is due to the balance of retrograde flow and diffusion, the former from flow towards the trailing edge and the latter effected by motors unbinding from actin. The higher the diffusion, the less motors of the respective isoform arrive at the trailing edge. For the estimated value of $K_r = 0.2$, isoform A has a larger effective diffusion than isoform B. Thus, B accumulates more quickly at the trailing edge. The effect of excluded volume then constrains A to accumulate further up front.

The symmetry breaking of concentration profiles is caused by the advection of myosin along the actin retrograde flow. The diffusion, depending on both K_r and c_∞, counteracts this by flattening the profiles. Hence, this polarization can only occur if the Péclet number is sufficiently large. This mechanism remains qualitatively unchanged when varying the other parameters. A more thorough sensitivity analysis of the parameters is performed in the appendix. The theoretical results agree with the experimental data from Weissenbruch *et al.* [15], compare Figs. 2(f) and 1(c).

The myosin isoforms are mobile within the cell and are transported with actin filaments in the retrograde actin flow. Using finite-volume simulations we can trace this flow $\tilde{v}$, introduced in Eq. (10) [43]. The result can be seen in Fig. 3 as a kymograph, showing a cell that, after an initial perturbation, approaches a state of steady motility to the left. The retrograde flow is directed towards the rear end of the cell with a typical speed of $\tilde{v}_{max} \sim 10^{-2}$ μm s^{-1}. This value is small but not unrealistic [55].

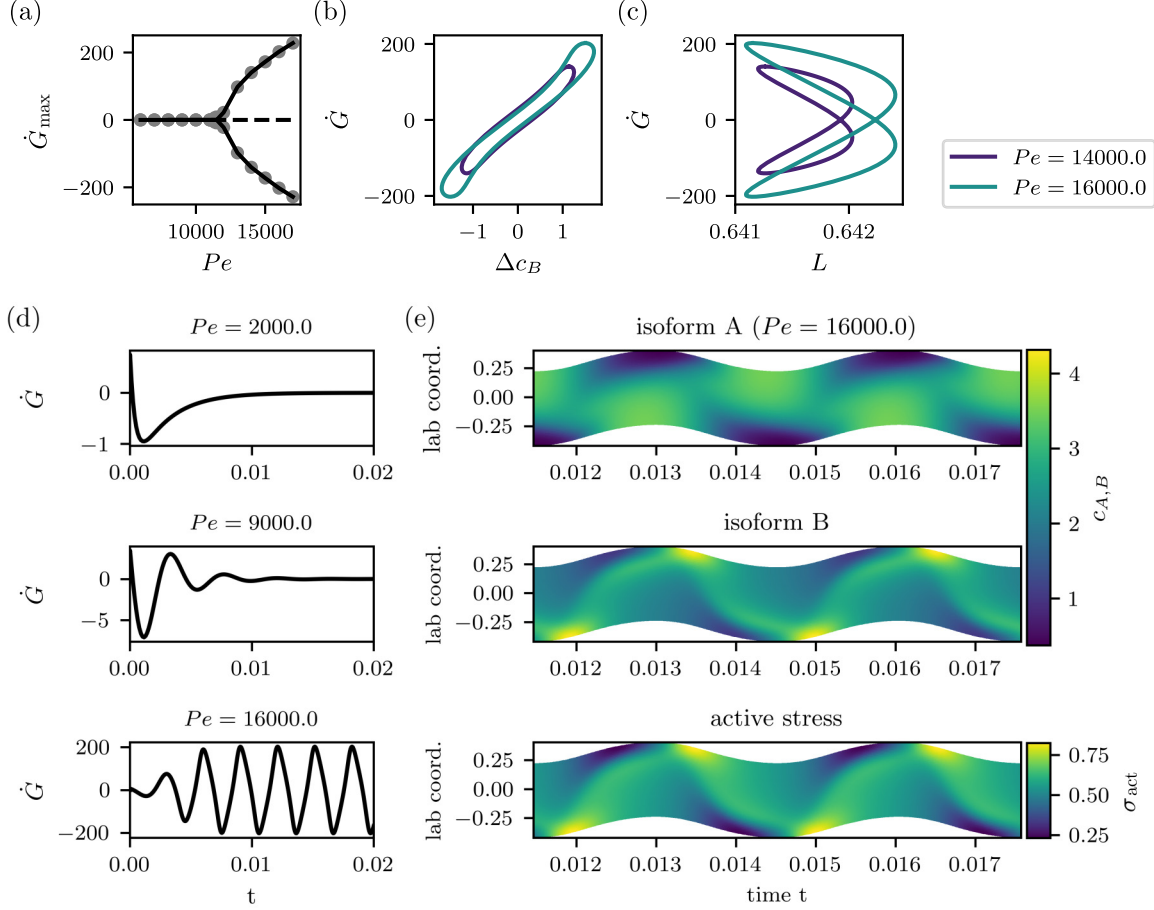FIG. 4. Oscillatory dynamics of the two isoform system. (a) Hopf bifurcation at $\mathcal{K}_{crit} = 11\,500$ in the $\dot{G}_{max}$-Pe plane, where $\dot{G}_{max}$ refers to the maximum velocity within an oscillation cycle. (b) Exemplary limit cycles in the $\dot{G}_{max}$-Δc_B plane, where $\Delta c_B = c_B(l_+) - c_B(l_-)$ is a measure of the polarity of the myosin B distribution. The size of the limit cycle grows with Pe. (c) Exemplary limit cycles in the plane cell velocity vs cell length. (d) Examples of the three different motility modes—sessile, transient oscillation, and stable oscillation. Shown is the cell velocity over time. (e) Kymographs visualizing the pull-push mechanism. Shown are the distributions of both myosin isoforms (upper and middle panel) and the resulting total active stress (lower panel) in a stable oscillatory state at Pe $= 16\,000$. Parameters as in Fig. 2, except for concentration ratio of $c_r = 1$ and strongly increased dissociation/diffusion ratio $K_r = 10$.

D. Exploring parameter space and occurrence of oscillations

We now lift the constraint of steady states, solving the full boundary value problem Eq. (10) numerically, and explore the parameter space beyond the values estimated from experiments. As in the polarization mechanism, the most interesting parameters to study are the ratio of the dissociation constants, K_r, the contractilities P_A and P_B, and the Péclet number. These parameters again qualitatively determine the motility mode of the system. In the following, we will keep the contractility values, but consider a large $K_r = 10$ instead of the low $K_r = 0.2$ from before. In this parameter regime, we find additional modes of motility, in particular the possibility of oscillations, as shown in Fig. 4. For small Péclet number Pe we again find stable sessile steady states. Increasing Pe leads to the onset of transient oscillations, whose amplitudes decay towards the sessile steady state in the regime $6000 \lesssim$ Pe $\lesssim 11\,500$. Beyond a critical value of Pe$_{crit} \approx 11\,500$, these oscillations prevail and become stable. This behavior can be traced back to a Hopf bifurcation as shown in Figs. 4(a)–4(c). Examples for the three different modes of motility—sessile,

transient oscillation and stable oscillation—are shown in Fig. 4(d).

For the oscillations to occur, the system requires a larger Péclet number. The increase of the critical Péclet number for the bifurcation as compared to Fig. 2 can be traced back to the increase of the effective diffusion of B (by a factor of 50) and the scaling of the Péclet number with the squared inverse of diffusion. The combination of the bifurcation diagram, cf. Fig. 2(a), and the growing closed limit cycles, cf. Figs. 2(b) and 2(c), demonstrate the emergence of a supercritical Hopf bifurcation towards stable oscillations. Compared to the cell velocity oscillations, the oscillations in cell length are smaller by several orders of magnitude, see Fig. 2(c).

It is also interesting to study the polarity, which can be quantified by the left-right edge difference of the stronger motor $\Delta c_B = c_B(1) - c_B(0)$. The polarity and the velocity oscillate with the same frequency; see Fig. 4(b). while the length oscillates with twice the frequency of the velocity oscillation, Fig. 4(c). This is because in each cycle the cell
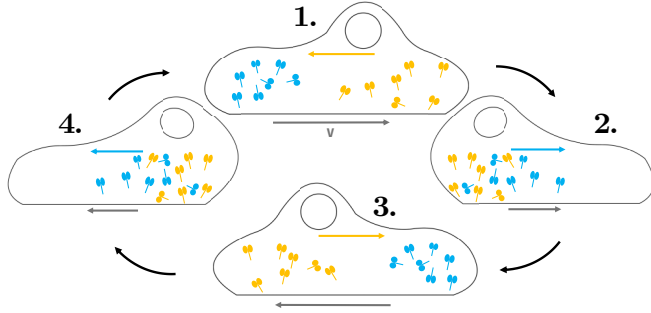
FIG. 5. Schematic sketch of myosin dynamics within an oscillating cell. (1) The cell initially moves to the right. More contractile species B (blue) at the back causes net flow of A (yellow) to the left. (2) Then A displaces B. Net flow of B to the right (blue arrow). (3) Cell movement slows down and reverses. Cycle of "pull-and-push" starts in the other direction.

passes every length twice, once during contraction and once during elongation. How can the mechanism of the oscillation be understood? One has to note that for $K_r > 0$, one myosin isoform (namely NMII B) is more diffusive and, because of our choice of parameters here, also more contractile. If we initially assume a spatial separation of both isoforms, then the stronger isoform B induces a larger—and hence dominating—contractile stress that induces an actin flow towards the position where isoform B is the most aggregated. Myosin motors of isoform A are advected along the retrograde actin flow. As an effect of volume exclusion, isoform A subsequently displaces the more diffusive isoform B from its initial position and effectively "pushes" it to the other side of the cell. From this point on the pull-and-push cycle repeats. A schematic sketch of the internal myosin dynamics during one oscillation cycle is depicted in Fig. 5.

This pull-push mechanism is clearly visible within the simulation data in Fig. 4(e), showing kymographs (space-time-plots) of both isoforms (upper and middle panel) and the total active stress (lower panel) driving the dynamics. One can see that both isoforms continuously exchange positions which in turn corresponds to an oscillatory active stress. Within the laboratory frame, the cell oscillates in space and velocity. As the oscillation in cell length are much smaller than the one in cell velocity, it is barely visible in the kymographs.

Increasing Pe $\gtrsim$ 17 000, our numerics, using a finite-volume method implemented with the FiPy-package for *python* [56], became numerically unstable. The reason is that at such high Péclet number, advection dominates the diffusion and causes a lack of regularization. A code better adapted to the hyperbolic nature of this regime could be developed. We have rather chosen to circumvent this numerical problem by considering the rigid limit of the boundary value problem in the following, which also sheds new light on the origin of the oscillation and allows to establish a state diagram for the system.

E. The rigid limit and the state diagram

The much smaller oscillation amplitude of the cell length compared to the cell velocity, cf. Fig. 4(c), suggests to look at the rigid limit of the problem, i.e., where the cell has constant length, to simplify the analysis.

Similarly as suggested in Ref. [20], we introduce a new dimensionless stress $\sigma' = \sigma/(c_A^0 \chi_A)$ leading to a new parameter for relative contractility $\chi_r = \chi_A/\chi_B$ and a new continuation parameter $\lambda = \text{Pe}P_A$. All other parameters from Eqs. (10) remain unchanged. The stiff limit then requires the contractility to be so small that the cell is not contracted, i.e., $P_{A,B} \to 0$, $L \to 1$. This leads to the adjusted elastic boundary condition

$$\sigma'(l_\pm, t) = \lim_{P_A \to 0} \lim_{L \to 1} \left(-\frac{1}{P_A}(L-1) \right) =: \sigma_0, \quad (11)$$

where we assume the parameter σ_0 to be finite and implicitly defined through the remaining boundary conditions. We thus exchange the dynamics of the length, L, with the one from an implicitly defined "background stress" σ_0, which encodes the changes in the averaged level of contraction.

To simplify the problem we introduce the stress deviation field $s(u) = \lambda(\sigma'(u) - \sigma_0)$. In internal coordinates, the new boundary value problem now reads

$$-\mathcal{L}^2 \partial_u^2 s + s + s_0 = \lambda\left(c_A + \frac{1}{\chi_r}c_B \right), \quad (12a)$$

$$\partial_t c_A = \partial_u[(\dot{G} - \partial_u s)c_A] + \partial_u \mathcal{D}_A(c_A, c_B), \quad (12b)$$

$$\partial_t c_B = \partial_u[(\dot{G} - \partial_u s)c_B] + K_r \partial_u \mathcal{D}_B(c_A, c_B), \quad (12c)$$

where $s_0 = \lambda\sigma_0$ and the diffusion coefficients are the ones from from Eq. (6). The boundary conditions now read $\partial_u c_{A,B}(u_\pm, t) = s(u_\pm) = 0$ and $\partial_u s(u_\pm) = \dot{l}_\pm \equiv \dot{G}$. Note that albeit having set the length to a constant value, which makes Eqs. (12) much simpler than Eqs. (10), we have not lost its degree of freedom, which is now encoded in the background stress s_0.

We can now perform a linear stability analysis, i.e., we expand all variables of our system in terms of small time- (and space-) dependent perturbations, added to the homogeneous steady state,

$$s_0(t) = s_0^0 + \delta s_0(t), \quad (13a)$$

$$s(u, t) = s^0 + \delta s(u, t), \quad (13b)$$

$$c_i(u, t) = c_i^0 + \delta c_i(u, t), \quad i = A, B. \quad (13c)$$

We now neglect any dynamics of the background stress by assuming $\delta s_0(t) \equiv 0$. From the stress boundary condition, we can infer $s^0 = 0$. The equilibrium values for the isoforms are chosen, as before, to be $c_A^0 = 1$ and $c_B^0 = c_A^0/c_r$. When solving Eqs. (12) numerically using the finite-volume method, we, however, keep the dependence on the background stress. It then has to be determined for every time step, such that all boundary conditions are satisfied. In the analytical treatment, the perturbations are decomposed into Fourier modes of the form $[X_i(q_i)\cos(q_i u) + Y_i(q_i)\sin(q_i u)]e^{\sigma_q t}$ that have to satisfy the boundary conditions, leading to

$$\delta s = Y_s(2n\pi)\sin(2n\pi u)e^{\sigma_q t}, \quad (14a)$$

$$\delta c_A = X_A(n\pi)\cos(n\pi u)e^{\sigma_q t}, \quad (14b)$$

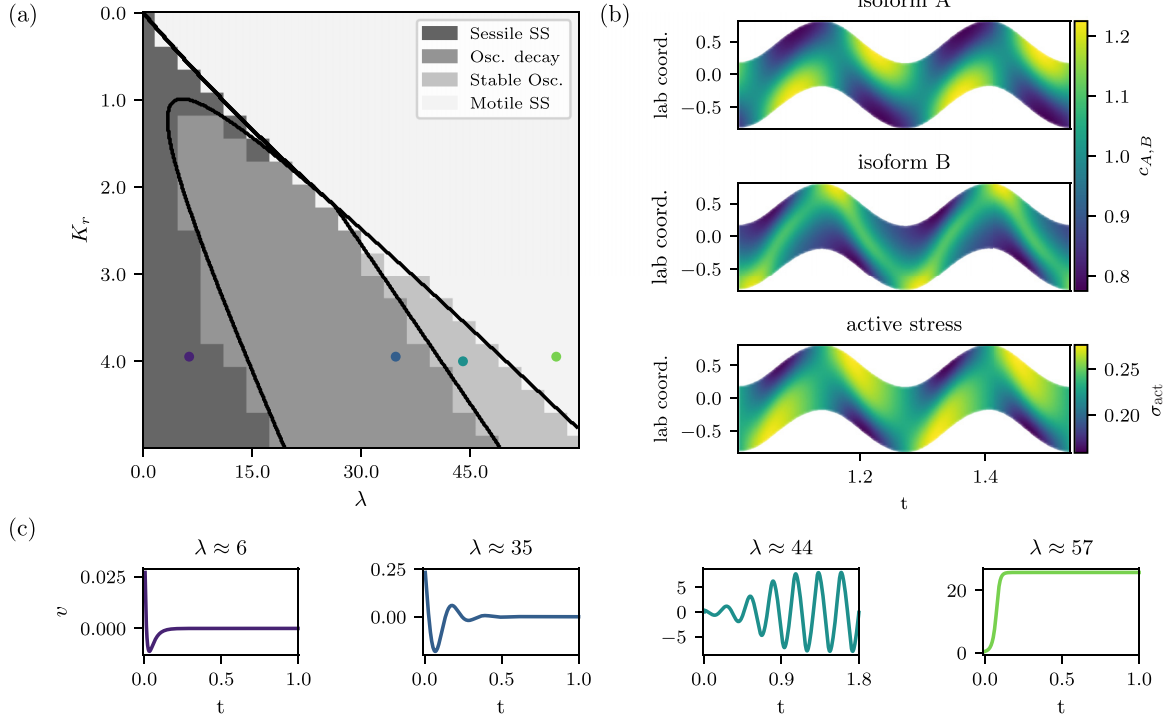$$\delta c_B = X_B(n\pi)\cos(n\pi u)e^{\sigma_q t}. \quad (14c)$$

FIG. 6. Motility modes in the rigid limit. (a) State diagram of the four different motility modes depending on the relative diffusion K_r vs the rescaled Péclet number λ. Numerical results obtained by finite-volume simulations of Eqs. (12) are coded in levels of gray. The curves are obtained from the linear stability eigenvalue problem and mark analytically predicted borders of the state diagram. (b) Kymographs for the two motor isoform concentrations and the resulting total active stress in a state of stable oscillations ($\lambda = 44$). (c) Examples of the four different motility modes as plots of velocity over time. λ is varied while $K_r \approx 4$ was kept fixed. Parameters correspond to the points indicated in (a). Parameters not mentioned have the same values as in Fig. 4.

The spectrum of wave vectors is discrete with $n \in \mathbb{N}$ as we consider the finite domain $u \in [0, 1]$. Expanding the system of Eqs. (12) to linear order in the perturbations and inserting Eqs. (14) we obtain an eigenvalue problem $\sigma_q \mathbf{X} = \mathbf{M}_q \mathbf{X}$ for the vector $\mathbf{X} = (\delta s, \delta c_A, \delta c_B)$, with the matrix

$$
\mathbf{M}_q = \begin{pmatrix} -4\mathcal{L}^2 q^2 - 1 & \lambda & \lambda/\chi_r \\ 4c_A^0 q^2 & -q^2 \frac{(c_\infty - c_B^0)}{\zeta_h} & -q^2 \frac{c_A^0}{\zeta_h} \\ 4c_B^0 q^2 & -q^2 K_r \frac{c_B^0}{\zeta_h} & -q^2 K_r \frac{(c_\infty - c_A^0)}{\zeta_h} \end{pmatrix}.
$$

(15)

In the submatrix of the myosin concentrations, we introduced the common factor $\zeta_h = (c_\infty - c_A^0 - c_B^0)^2/c_\infty$ coming from the nonlinear diffusion. The construction of the matrix $\mathbf{M}_q$ through first- and second-order partial derivatives with respect to the perturbed variables renders the constant term s_0^0 irrelevant.

To predict the different modes of motility, we have to solve the eigenvalue problem. It is important to note that Eq. (12a) does not have any time derivatives, and hence we take $\sigma_q = 0$ in the first row of the characteristic equation. This effectively sets one eigenvalue to zero and we are left with a pair of eigenvalues that potentially are complex.

The results are shown in Fig. 6. As shown in Fig. 6(a), the numerical results of the full system of Eqs. (12)—shown as background colors—agree very well with the linear stability analysis (curves). This *a posteriori* justifies the neglect of

perturbations in s_0. We can identify four different modes of motility: sessile steady states, oscillations decaying towards a sessile steady state (transient oscillations), stable oscillations, and motile steady states. Exemplary plots of velocity as a function of time for each of these modes are shown in Fig. 6(c).

As also obvious from Fig. 6(a), oscillations can only occur in case of $K_r > 1$. This implies $K_A > K_B$, meaning that the stronger isoform (myosin B) must have larger effective diffusion than the weaker isoform (myosin A). In the case of stable oscillations, we recover the pull-push mechanism that includes the consecutive displacement among both isoforms as shown in the kymograph of Fig. 6(b). This again proves the qualitative consistency of the rigid limit with the initial model, Eq. (10).

Note that in the linear analysis we have only used the first mode ($n = 1$), as it is the most dominant one for the dynamics at the given hydrodynamic length of $\mathcal{L} \sim 1.25$: In fact, it is the first antisymmetric mode that creates the strongest polarity for δc_A and δc_B. Modes of even n do not produce cell motility as they create symmetric concentration profiles. Higher modes of odd n cause antisymmetric concentration profiles that consist of multiple maxima/minima, leading to overall less polarity. Hence, the first mode suffices for a qualitative analysis of the dynamics of the system, as also confirmed by the numerical solution. Also note that performing an analogous linear stability analysis for the original system Eq. (10) by simply fixing the length does not

yield results consistent with the corresponding finite-volume simulations.

F. Effect of actin polymerization

Contraction-driven motility emerges by an internal symmetry break as explained above. Uneven actin polymerization at the cell boundaries breaks front-rear symmetry by construction and allows cells to quickly respond to external cues. For one-species models, this effect of actin polymerization has been demonstrated before [20–22]. Although here our focus is on contractility, for completeness we have also performed a similar analysis for the two-species model presented here. Polymerization can be incorporated into our model by modifying the force balance equation of Eq. (2) adding the constant polymerization velocity v_p to the contraction driven velocity $v(l_\pm)$ at the cell edges

$$\dot{l}_\pm = \frac{1}{\xi}\partial_x\sigma(l_\pm(t),t) + v_p. \tag{16}$$

This corresponds to symmetric polymerization where actin filaments are extended at the leading and retracted at the trailing edge with the same speed. In order to keep the total mass of myosin constant, polymerization requires novel flux boundary conditions,

$$\partial_x c_{A,B}(l_\pm,t) = -\frac{v_p}{D}\frac{(c_\infty - c_{A,B}(l_\pm,t))^2}{c_{A,B}(l_\pm,t)}. \tag{17}$$

This change poses difficulties when formulating the equations for steady-state motility as additional boundary terms are required. In the following analysis, we focus on the steady-state equations previously derived under no-flux boundary conditions. As a result, there is a slight loss of total myosin mass; however, this effect remains negligible for small polymerization velocities and over short timescales. While this approach is approximate, it nonetheless offers valuable qualitative insight into the system's behavior. Figures 7(a) and 7(b) show the bifurcation analysis in steady state subject to small polymerization velocities. Any nonzero polymerization turns the pitchfork bifurcation into an imperfect bifurcation, which means that it splits into a biased motile solution branch, a stable solution branch with opposite polymerization- and contraction-driven polarizations, and an unstable branch unpolarized in the myosin distribution except for retrograde flow from polymerization. This change in bifurcation type, however, neither changes the polarization mechanism from contraction nor the qualitative isoform distribution [cf. Fig. 7(c)].

IV. DISCUSSION

Motivated by the existence of several isoforms of NMII, and specifically by the experiments by Weissenbruch *et al.* [15,16], we have developed and analyzed a physical model including two interacting isoforms of NMII proteins. The interaction between the myosin isoforms A and B is mediated by excluded volume, that depends on the saturation concentration and leads to nonlinear diffusion, derived both via a microscopic binding kinetics and nonequilibrium thermodynamics. The corresponding physics is that of a Tonks gas. In the future,
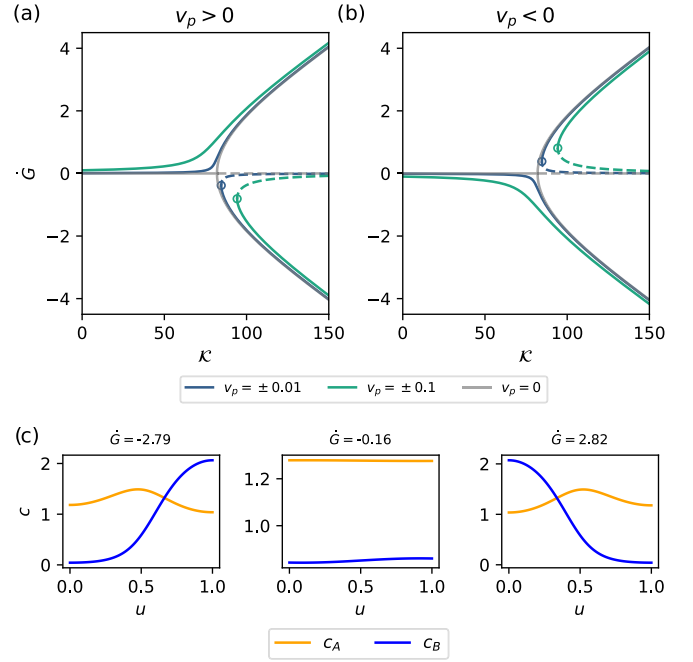

FIG. 7. Bifurcation diagrams for different polymerization velocities v_p. As soon as $v_p \neq 0$ the symmetry of the supercritical pitchfork bifurcation is broken and imperfect bifurcations with three branches emerge. (a) Bifurcation diagram for positive v_p. (b) Bifurcation diagrams for negative v_p. Encircled points mark changes in stability. (c) Concentration profiles taken at $\mathcal{K} = 120$ for polymerization velocity $v_p = 0.01$ at the stable solution branch, the unstable branch and the biased motile solutions (from left to right). Parameters used: $\mathcal{L}^2 = 1.25$, $K_r = 0.2$, $P_A = 0.05$, $P_B = 0.18$, $c_\infty = 4$, $c_r = 1.5$.

one could also include an attractive interaction, thus changing to the van der Waals fluid as a reference case, as suggested earlier for a one-species active gel model [22]. We expect that such a model extension would change the bifurcation from supercritical to subcritical, leading to bistability and the possibility of optogenetic switching. Because this is not the focus of the current work and would make analytical progress even more difficult; here we did not study this potential extension.

The two-species model introduced here recovers the experimental distributions of the isoforms and in addition predicts the existence of a variety of migratory modes. Regarding the steady states, in the nonmotile steady state both isoforms are homogeneously distributed and cause a symmetric active contractile stress. At sufficiently large Péclet numbers; however, this symmetry is broken and polarized concentration fields and, consequently, polarized active stress profiles emerge. This onset of polarization and migration is due to a supercritical pitchfork bifurcation. For a steadily moving cell beyond the bifurcation, we find the experimentally observed, isoform-specific myosin distribution profiles [15]: The faster NMIIA accumulates at the leading edge, while the stronger NMIIB localizes at the trailing edge. We also showed that our model can be extended to describe the effect of uneven actin polymerization at the boundaries, which immediately stabilizes motile solutions and leads to an imperfect pitchfork bifurcation but otherwise does not change our conclusions.
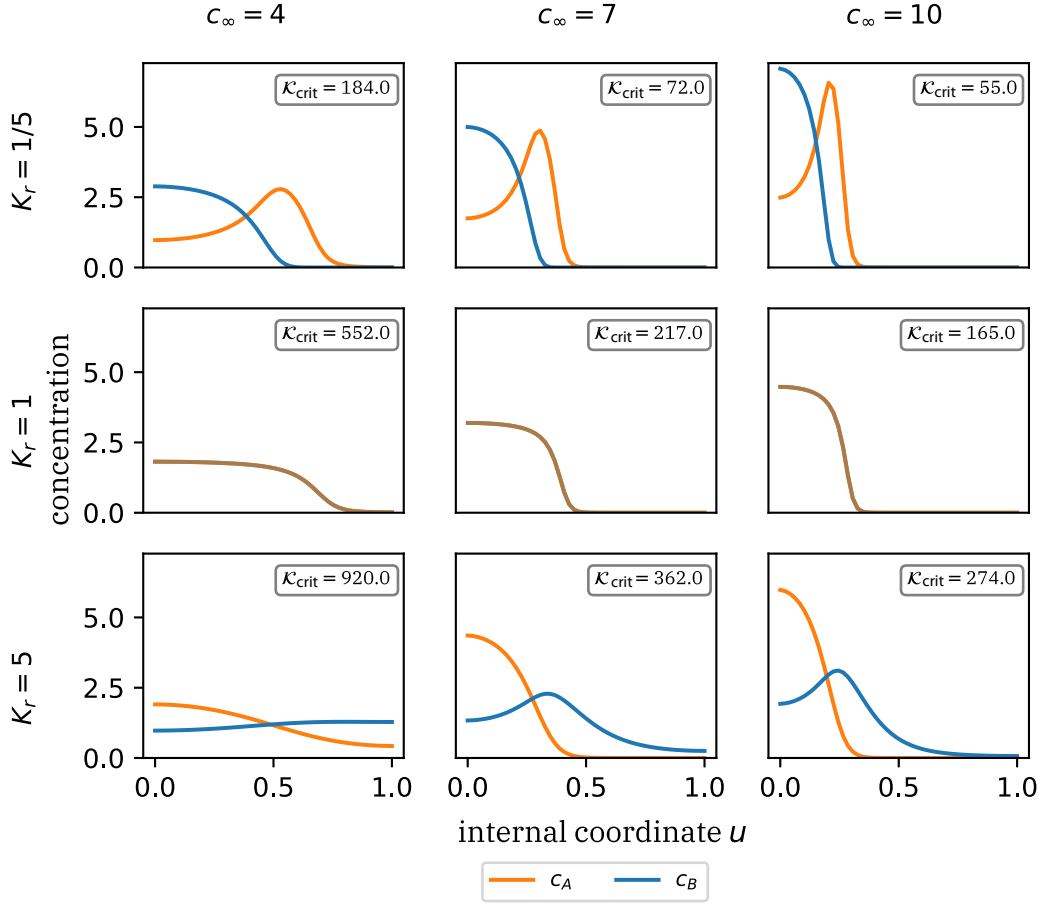
FIG. 8. Concentration profiles for different saturation concentrations c_∞ and relative diffusivities K_r. All profiles taken at $\mathcal{K} = 1000$, contractilities $P_A = P_B = 0.06$ and total concentration ratio $c_r = 1$. For $K_r = 1$ both profiles are equal.

Our one-dimensional model is motivated by the recent body of experimental work of cells migrating along lines and in channels. In order to analyze higher dimensions, other model classes such as phase field models are easier to implement [8,57], although a recent mathematical analysis showed how a rigorous bifurcation analysis can be performed on a 2D model similar to the one described here [44]. Due to the similarities of this work with the one-dimensional one-species model [21], we would also expect our two-species model to behave similarly in two dimensions.

We have explored further modes of motility besides the steady-state solutions. Oscillations occur in case that the more contractile isoform is also more diffusive (i.e., $P_B > P_A$, $K_r > 1$), via a cyclic pull-push mechanism. This mechanism works best for similar total abundances of both isoform, $c_r \sim$ 1. It has been suggested that different myosin isoforms can be regulated independently [58–60], which would allow for the relative diffusion to be controlled via K_r. Albeit not observed in the animal cell type investigated in Refs. [15,16], it is not unlikely that these oscillations might occur in other cell types (e.g., from other species). Another interesting option is to genetically engineer cells such that these oscillations occur, either spontaneously or triggered by external control, in particular by optogenetics. If oscillations can be controlled in this manner, then it also would be easy to distinguish them

from oscillations that occur as a result of nonlinear friction, as described by clutch models [61–63].

In the oscillatory state, the amplitude of the cell length oscillation is much smaller than the one of velocity. This suggested to study the rigid limit, which enabled an analytic linear stability analysis and allowed to determine the full state diagram of the system, containing sessile cells, cells with transient oscillations and persistent oscillations, as well as steady motile cell solutions. This phase diagram is in good agreement with finite-volume simulations of the full model.

In summary, here we have shown that active gel theory can be extended to also describe the effect of having two complementary isoforms at work. The fact that we could derive the same model from both kinetic and a thermodynamic perspectives demonstrate its fundamental nature and paves the way to also include other biologically relevant effects into the model. In particular, a third major molecular constituent of contractile structures in cells is α-actinin, which like NMII also exists in different isoforms and which also competes for binding to the actin filaments. In our model framework, such a competitor would increase excluded volume for the NMII and therefore decrease active stress. At the same time, α-actinin might increase elasticity and therefore make the cell effectively stiffer. It would be interesting to include such effects, but this also would introduce many more model parameters,
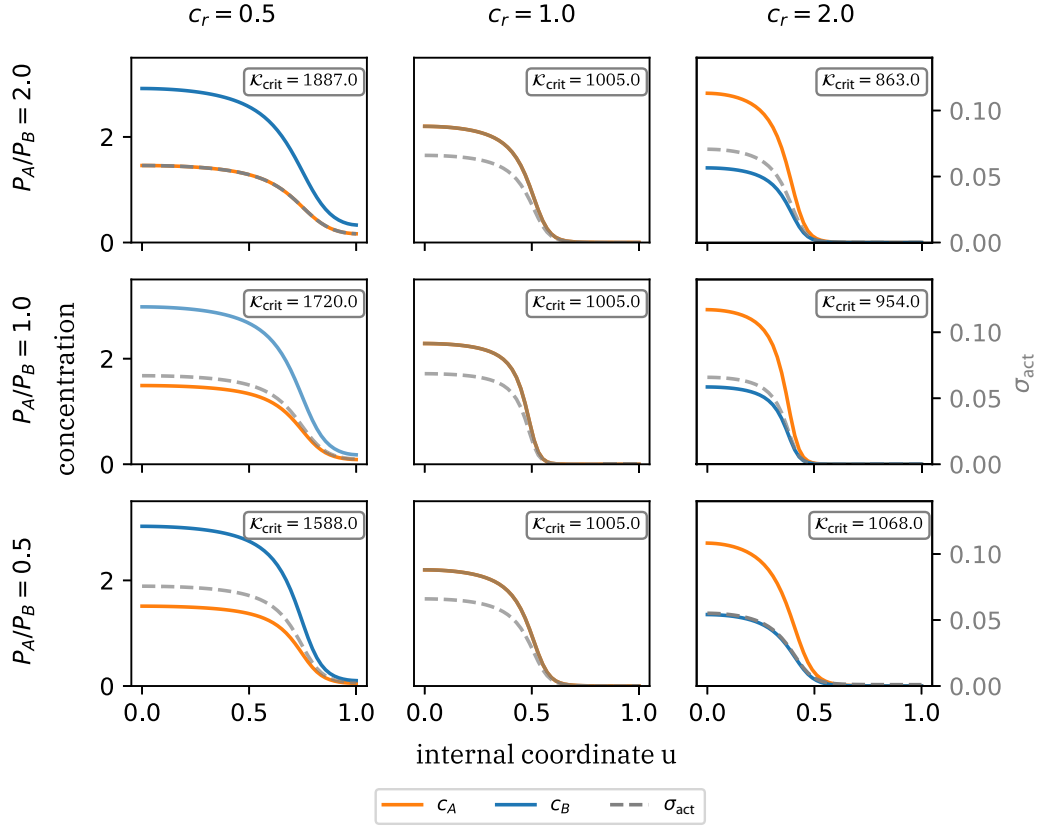
FIG. 9. Concentration profiles and active stress for varying relative contractility and concentration ratios. All profiles are plotted at $\mathcal{K} = 2500$. Fixed parameters are $K_r = 1.0$, $c_\infty = 5$. The following values for the respective contractility were used: first row: $P_A = 0.02$, $P_B = 0.01$; second row: $P_A = P_B = 0.015$; third row: $P_A = 0.01$, $P_B = 0.02$.

that then had to be estimated from experiment. The same is true for replacing the simple friction by a molecular clutch [61,64]. Despite this complexity, however, the work presented here clearly shows that molecular details can be fruitfully included in fundamental models for cell motility.

DATA AVAILABILITY

The data that support the findings of this article are openly available [43].

APPENDIX: PARAMETER ANALYSIS

In the following, we analyze the system's dependence on several parameters and their effect on the dynamics. We use steady-state solutions throughout. For all analyzed values we find supercritical pitchfork bifurcations at $\mathcal{K}_{\text{crit}}$ in analogy to what is shown in Fig. 2(a).

Figure 8 shows the effect of various combinations of parameter values of saturation concentration c_∞ and relative diffusivity K_r. Following the rows, we see that a low saturation concentration flattens and widens the concentration profiles. In contrast, high saturation allows for sharper peaks and overall spatially narrower profiles inside the cell. This holds for all K_r. Larger saturation concentrations allow for stronger polarization at the edges. Hence, the bifurcation point $\mathcal{K}_{\text{crit}}$ marking the transition from sessile to motile states shifts to smaller values for increasing saturation concentration. The columns reveal the influence of relative diffusion. The isoform with the lowest diffusivity sits further in the back (species B for $K_r < 0$, species A for $K_r > 0$). We can explain this by the transport of myosin along the retrograde actin flow. The retrograde flow moves towards the trailing edge. For the cases depicted here of positive cell velocity we find a flow towards the left. During advection, the motors also diffuse away and unbind from actin. The higher the diffusion, the less motors arrive at the trailing edge to initiate motility. This also explains why the critical Péclet number ($\mathcal{K}_{\text{crit}}$) increases with increasing K_r. According to Eq. (10), the diffusion of species A is not affected by K_r, which only influences the diffusion of species B. Hence, an increase in K_r leads to a higher total diffusion with less biased concentration and therefore less asymmetric active stress profiles, causing a later onset of motility. Once

the space at the trailing edge is occupied by the less diffusive species, the other species can only place itself closer to the cell center due to the volume exclusion interaction.

Figure 9 shows the effect of varying the ratio of total concentration and the ratio of contractility. Since K_r is kept constant the concentration profiles of A and B have a similar qualitative shape and positions in each respective plot. The relative magnitudes of the concentrations originate from c_r. For $c_\infty \neq 0$ one species is more abundant—species A when $c_r > 1$, species B when $c_r < 1$ while for $c_r = 1$, the profiles and the active stress σ_{act} are also quantitatively equal. For all plots, the sum of both contractilities is equal. For each row, we find the narrowest and sharpest concentration profiles in the last column at the maximum and the flattest and broadest profiles in the first column at the minimum value of c_r. The varying profile widths can be explained by the way that we have normalized the concentrations: In internal coordinates $c_A^0 = 1$

and $c_B^0 = 1/c_r$. Hence, we find the highest sum of integrated concentrations for $c_r = 0.5$ and the lowest for $c_r = 2.0$ ($c_A^0 + c_B^0 = 3$, respectively, 1.5). Consequently, two phenomena can be identified. First, at low c_r (effective larger total concentration) the system is more significantly affected by the saturation concentration. The intensified repulsive volume exclusion force leads to flattening and broadening of the profiles. Second, for a larger total number of motors, increased myosin advection is required to facilitate polarization, as can also be seen in the shifting bifurcation point $\mathcal{K}_{\mathrm{crit}}$. With an increase in c_r, a decreasing trend in $\mathcal{K}_{\mathrm{crit}}$ is observed. An exception to this trend appears in the final plot of the last row. There, the combination of A being more abundant while B is more contractile leads to a higher critical Péclet number. The influence of the contractility ratio on the shapes and magnitudes of the concentration is negligible.

[1] G. Reig, E. Pulgar, and M. L. Concha, Development (Cambr. England) **141**, 1999 (2014).

[2] X. Trepat, M. R. Wasserman, T. E. Angelini, E. Millet, D. A. Weitz, J. P. Butler, and J. J. Fredberg, Nat. Phys. **5**, 426 (2009).

[3] S. Nourshargh, P. L. Hordijk, and M. Sixt, Nat. Rev. Mol. Cell Biol. **11**, 366 (2010).

[4] C. Stuelten, C. Parent, and D. Montell, Nat. Rev. Cancer **18**, 296 (2018).

[5] L. Blanchoin, R. Boujemaa-Paterski, C. Sykes, and J. Plastino, Physiol. Rev. **94**, 235 (2014).

[6] A. B. Verkhovsky, T. M. Svitkina, and G. G. Borisy, Curr. Biol. **9**, 11 (1999).

[7] A. J. Ridley, M. A. Schwartz, K. Burridge, R. A. Firtel, M. H. Ginsberg, G. Borisy, J. T. Parsons, and A. R. Horwitz, Science **302**, 1704 (2003).

[8] F. Ziebert, S. Swaminathan, and I. S. Aranson, J. R. Soc. Interface **9**, 1084 (2012).

[9] A. Hadjitheodorou, G. R. R. Bell, F. Ellett, S. Shastry, D. Irimia, S. R. Collins, and J. A. Theriot, Nat. Commun. **12**, 6619 (2021).

[10] L. Valon, A. Marín-Llaurado, T. Wyatt, G. Charras, and X. Trepat, Nat. Commun. **8**, 14396 (2017).

[11] K. Hennig, I. Wang, P. Moreau, L. Valon, S. DeBeco, M. Coppey, Y. A. Miroshnikova, C. Albiges-Rizo, C. Favard, R. Voituriez, and M. Balland, Sci. Adv. **6**, eaau5670 (2020).

[12] M. Vicente-Manzanares, X. Ma, Adelstein et al., Nat. Rev. Mol. Cell Biol. **10**, 778 (2009).

[13] K. Weißenbruch and R. Mayor, BioEssays **46**, 2400055 (2024).

[14] J. R. Beach, L. Shao, K. Remmert, D. Li, E. Betzig, and J. A. Hammer, Curr. Biol. **24**, 1160 (2014).

[15] K. Weißenbruch, M. Fladung, J. Grewe, L. Baulesch, U. S. Schwarz, and M. Bastmeyer, Eur. J. Cell Biol. **101**, 151213 (2022).

[16] K. Weißenbruch, J. Grewe, M. Hippler, M. Fladung, M. Tremmel, K. Stricker, U. S. Schwarz, and M. Bastmeyer, eLife **10**, e71888 (2021).

[17] K. Kruse, J. F. Joanny, F. Jülicher, J. Prost, and K. Sekimoto, Phys. Rev. Lett. **92**, 078101 (2004).

[18] K. Kruse, J. Joanny, F. Jülicher et al., Eur. Phys. J. E **16**, 5 (2005).

[19] P. Recho, T. Putelat, and L. Truskinovsky, Phys. Rev. Lett. **111**, 108102 (2013).

[20] P. Recho, T. Putelat, and L. Truskinovsky, J. Mech. Phys. Solids **84**, 469 (2015).

[21] O. M. Drozdowski, F. Ziebert, and U. S. Schwarz, Phys. Rev. E **104**, 024406 (2021).

[22] O. M. Drozdowski, F. Ziebert, and U. S. Schwarz, Commun. Phys. **6**, 158 (2023).

[23] L. Tonks, Phys. Rev. **50**, 955 (1936).

[24] J. S. Bois, F. Jülicher, and S. W. Grill, Phys. Rev. Lett. **106**, 028103 (2011).

[25] M. A. Geeves and K. C. Holmes, Adv. Protein Chem. **71**, 161 (2005).

[26] H. L. Sweeney and A. Houdusse, Annu. Rev. Biophys. **39** 539 (2010).

[27] T. Erdmann, P. J. Albert, and U. S. Schwarz, J. Chem. Phys. **139**, 175104 (2013).

[28] T. Erdmann, K. Bartelheimer, and U. S. Schwarz, Phys. Rev. E **94**, 052403 (2016).

[29] S. Stam, J. Alberts, M. L. Gardel, and E. Munro, Biophys. J. **108**, 1997 (2015).

[30] J. Müller and W. van Saarloos, Phys. Rev. E **65**, 061111 (2002).

[31] H. Chelly and P. Recho, Phys. Rev. E **105**, 064401 (2022).

[32] D. G. Leaist and S. M. Abdu, J. Chem. Eng. Data **46**, 922 (2001).

[33] A. Vergara, L. Paduano, and R. Sartorio, Macromolecules **35**, 1389 (2002).

[34] V. K. Vanag and I. R. Epstein, Phys. Chem. Chem. Phys. **11**, 897 (2009).

[35] P. Tarazona, J. Cuesta, and Y. Martinez-Raton, Lect. Notes Phys. **753**, 247 (2008).

[36] P. Tarazona and Y. Rosenfeld, Free energy density functional from 0D cavities, in *New Approaches to Problems in Liquid State Theory*. NATO Science Series Vol 529, edited by C. Caccamo, J. P. Hansen, and G. Stell (Springer, Dordrecht, 1999).

[37] L. Lafuente and J. A. Cuesta, Phys. Rev. Lett. **89**, 145701 (2002).

[38] L. Lafuente and J. A. Cuesta, Phys. Rev. Lett. **93**, 130603 (2004).

[39] P.-G. de Gennes, Polymer solutions in good solvents, in *Scaling Concepts in Polymer Physics* (Cornell University Press, Ithaca, New York, 1979).

[40] K. A. Dill and S. Bromberg, Polymer solutions, in *Molecular Driving Forces—Statistical Thermodynamics in Chemistry and Biology* (Garland Science, New York, 2002).

[41] T. Aslyamov, F. Avanzini, E. Fodor, and M. Esposito, Phys. Rev. Lett. **131**, 138301 (2023).

[42] M. Mayer, M. Depken, J. S. Bois, F. Jülicher, and S. W. Grill, Nature (London) **467**, 617 (2010).

[43] N. O. Winkler, O. M. Drozdowski, F. Ziebert, and U. S. Schwarz, Computer code for numerical continuation and finite volume simulations (2025), https://github.com/winklernils/isoforms.

[44] L. Berlyand, O. Krupchytskyi, and T. Laux, arXiv:2506.03138 (2025).

[45] E. L. Barnhart, K.-C. Lee, K. Keren, A. Mogilner, and J. A. Theriot, PLoS Biol. **9**, e1001059 (2011).

[46] E. L. Barnhart, G. M. Allen, F. Jülicher, and J. A. Theriot, Biophys. J. **98**, 933 (2010).

[47] A. J. Loosley and J. X. Tang, Phys. Rev. E **86**, 031908 (2012).

[48] R. Uehara, G. Goshima, I. Mabuchi, R. D. Vale, J. A. Spudich, and E. R. Griffis, Curr. Biol. **20**, 1080 (2010).

[49] T. Luo, K. Mohan, V. Srivastava, Y. Ren, P. A. Iglesias, and D. N. Robinson, Biophys. J. **102**, 238 (2012).

[50] J. Kolega and D. L. Taylor, Mol. Biol. Cell **4**, 819 (1993).

[51] Y. Chen, D. Saintillan, and P. Rangamani, PRX Life **1**, 023007 (2023).

[52] S. Walcott, D. M. Warshaw, and E. P. Debold, Biophys. J. **103**, 501 (2012).

[53] A. Vilfan and T. Duke, Biophys. J. **85**, 818 (2003).

[54] E. J. Doedel and B. E. Oldeman, Auto-07p : Continuation and bifurcation software for ordinary differential equations (2012), https://github.com/auto-07p/auto-07p.

[55] A. Mogilner, E. L. Barnhart, and K. Keren, Semin. Cell Dev. Biol. **100**, 143 (2020).

[56] J. Guyer, D. Wheeler, and J. Warren, Comput. Sci. Eng. **11**, 6 (2009).

[57] F. Ziebert, J. Loeber, and I. S. Aranson, Macroscopic model of substrate-based cell motility, in *Physical Models of Cell Motility*, edited by I. S. Aranson (Springer International, Cham, 2016), pp. 1–67.

[58] A. R. Bresnick, Curr. Opin. Cell Biol. **11**, 26 (1999).

[59] B. Barua, D. A. Winkelmann, H. D. White, and S. E. Hitchcock-DeGregori, Proc. Natl. Acad. Sci. USA **109**, 18425 (2012).

[60] J. E. Clayton, M. R. Sammons, B. C. Stark, A. R. Hodges, and M. Lord, Curr. Biol. **20**, 1423 (2010).

[61] P. Sens, Proc. Natl. Acad. Sci. USA **117**, 24670 (2020).

[62] B. Amiri, J. C. Heyn, C. Schreiber, J. O. Rädler, and M. Falcke, Biophysical Journal **122**, 753 (2023).

[63] J. E. Ron, P. Monzo, N. C. Gauthier, R. Voituriez, and N. S. Gov, Phys. Rev. Res. **2**, 033237 (2020).

[64] V. Wössner, O. M. Drozdowski, F. Ziebert, and U. S. Schwarz, New J. Phys. **26**, 073039 (2024).